Supporting Information for “Atmospheric CO_2 and sea surface temperature variability cannot explain recent decadal variability of the ocean CO_2 sink”

Tim DeVries

[1]Department of Geography, University of California, Santa Barbara, CA 93106, USA.

[2]Earth Research Institute, University of California, Santa Barbara, CA 93106, USA.

Contents of this file

1. Supplemental Text
2. Table S1
3. Figures S1–S7

1. Supplemental Text

1.1. OCIM2-48L data constraints

The version of the OCIM used here (OCIM2-48L) assimilates six different circulation tracers: potential temperature, salinity, natural radiocarbon (Δ^{14}C), CFC-11, CFC-12, and natural δ^3He. Potential temperature and salinity observations are taken from the World Ocean Atlas 2013 (Locarnini et al., 2013; Zweng et al., 2013) annual mean objectively analyzed maps. We use the same compilation of Δ^{14}C observations used by

DeVries and Holzer (2019). This compilation includes data taken from the Global Ocean Data Analysis Project v2 (GLODAPv2) (Olsen et al., 2016), a compilation of Δ^{14}C measurements from surface corals (Guilderson et al., 2005), historical Δ^{14}C (Graven et al., 2012), and a collection of prebomb surface ocean radiocarbon measurements from the 14CHRONO database (available at `http://calib.org/marine/`). These observations were processed using exactly the same procedure as used in the OCIM2 (DeVries & Holzer, 2019), which includes screening for and removal of observations that are potentially contaminated by bomb radiocarbon. CFC-11 and CFC-12 measurements were taken from the GLODAPv2 database (Olsen et al., 2016). Helium isotope (δ^3He) data were taken from GLODAPv2 database (Olsen et al., 2016) and screened to remove bomb-contaminated data as described in (DeVries & Holzer, 2019). The OCIM also assimilates the climatological average air-sea heat and freshwater fluxes from the NCEP reanalysis for the period 1980-2009 (Behringer & Xue, 2004) as well as the mean dynamical sea surface topography from the AVISO mean dynamic topography product for the period 1993-1999 (release MDT-CNES_CLS09). The assimilation is accomplished by adjusting model parameters to minimize a quadratic cost function that measures the misfit between the model and observations, as in previous versions of the OCIM (DeVries & Primeau, 2011; DeVries, 2014; DeVries & Holzer, 2019). Figure S1 shows a comparison of modeled and observed tracers for the Atlantic Ocean.

1.2. OCIM updates

The differences between the OCIM2-48L and the OCIM1 that was used in a previous study to estimate ocean anthropogenic carbon uptake (DeVries, 2014) are as follows:

1. The vertical resolution has been increased from 24 vertical levels to 48 vertical levels. The thickness of these layers varies from $\sim$10 m near the surface to $\sim$300 m in the deepest ocean.

2. The vertical diffusivity is parameterized using a new model of tidal energy dissipation (de Lavergne et al., 2019, 2020). This model predicts the global distribution of energy dissipation in the ocean due to the breaking of internal waves generated by tides flowing over rough topography. The OCIM retains enhanced vertical diffusivities in the surface mixed layer that are parameterized using the KPP scheme (Large et al., 1994), as implemented by DeVries (2014).

3. The isopycnal diffusivity is determined as part of the solution to the inverse model, rather than being specified *a priori*.

4. The surface mixed layer is prescribed using the annual-average mixed layer depth, rather than the monthly maximum mixed layer depth. This choice was made to more accurately reflect the annual-average subduction of CO_2 below the mixed layer, since the OCIM lacks any seasonality in circulation.

5. CFC-12 is used an additional tracer constraint on the inverse model solution.

6. Radiocarbon ($\Delta^{14}C$) is modeled using an explicit formulation of the 14C air-sea gas exchange, as in the most recent version of the OCIM (DeVries & Holzer, 2019). This contrasts with the version of OCIM used by (DeVries, 2014), which simulated radiocarbon by restoring to preindustrial surface $\Delta^{14}C$ values estimated by the Global Ocean Data Analysis Project (GLODAP). The approach taken here has been shown to more accurately reproduce the observed $\Delta^{14}C$ distribution (DeVries & Holzer, 2019).

7. Natural δ^3He is used as an additional tracer constraint on the inverse model solution. This has shown to improve the representation of interior-to-surface ventilation pathways and the abyssal circulation (DeVries & Holzer, 2019).

1.3. Inputs used for the CO_2 simulations with OCIM2-48L

Previous studies of anthropogenic CO_2 uptake with the OCIM1 used a globally-constant atmospheric pCO_2 and a yearly time-step, neglecting seasonality in atmospheric pCO_2 (DeVries, 2014). Here, a spatially- and seasonally-varying atmospheric pCO_2 is used. $pCO_{2,air}$ is a 3-dimensional field (latitude×longitude×time) that describes the spatial and temporal evolution of atmospheric pCO_2, which in turn is the product of the atmospheric CO_2 concentration, $x\mathrm{CO}_2$, and the sea level pressure, P_{atm},

$$p\mathrm{CO}_{2,air} = x\mathrm{CO}_2 \times P_{atm}. \qquad (1)$$

To create a 3-dimensional field of $x\mathrm{CO}_2$, a time series of $x\mathrm{CO}_2$ is created from 1780-2020 at four locations: South Pole (latitude 90°S; available at `ftp://aftp.cmdl.noaa.gov/data/trace_gases/co2/flask/surface/co2_spo_surface-flask_1_ccgg_month.txt`), American Samoa (latitude 14.3°S; available at `ftp://aftp.cmdl.noaa.gov/data/trace_gases/co2/flask/surface/co2_smo_surface-flask_1_ccgg_month.txt`), Mauna Loa (latitude 19.5°N; available at `ftp://aftp.cmdl.noaa.gov/data/trace_gases/co2/flask/surface/co2_mlo_surface-flask_1_ccgg_month.txt`), and Barrow, Alaska (latitude 71.3°N; available at `ftp://aftp.cmdl.noaa.gov/data/trace_gases/co2/flask/surface/co2_brw_surface-flask_1_ccgg_month.txt`). For the years 1977-2020, there are monthly measurements of $x\mathrm{CO}_2$ at each of these locations from NOAA monitoring stations (Dlugokencky et al., 2020). For the time period 1958-1977, there are monthly

xCO$_2$ measurements from Mauna Loa, but not from the other stations. To extend the time-series from these other stations back to 1958, a linear trend of the difference between the annual mean xCO$_2$ at each station (South Pole, American Samoa, and Barrow) and the annual mean xCO$_2$ at Mauna Loa, is fit over the time period 1977-2020, and this trend is extrapolated back to 1958. The annual mean xCO$_2$ at each station is then determined by adding this extrapolated difference to the annual mean xCO$_2$ from Mauna Loa, and the average monthly xCO$_2$ anomaly from 1977-2020 at each individual station is then added to the annual mean xCO$_2$ values to create a monthly time series at each station. The annual mean values of xCO$_2$ at each station in 1958 are similar, ranging from 315 ppm at South Pole to 317 ppm at Barrow, Alaska (Figure S2). These time-series are extended further back to 1700 using ice core CO$_2$ concentrations from the Law Dome ice core (Macfarling Meure et al., 2006) (data available at `https://scrippsco2.ucsd.edu/assets/data/atmospheric/merged_ice_core_mlo_spo/merged_ice_core_yearly.csv`), and assuming that the annual mean xCO$_2$ is the same at each station prior to 1958. The average monthly CO$_2$ anomalies from each station are added to the annual mean ice core xCO$_2$ values to create a monthly time-series at each station extending back to 1700 (Figure S2). Finally, this monthly time-series for these four stations is used to create a global xCO$_2$ time-series by linearly interpolating across latitude, and assuming that xCO$_2$ is zonally uniform. Last, the pCO$_2$ is calculated using equation (1) and P_{atm} from the National Centers for Environmental Prediction (NCEP) monthly reanalysis sea level pressure (Kalnay et al., 1996), which covers the time domain 1948-2020 (data available at `https://psl.noaa.gov/thredds/`

`catalog/Datasets/ncep.reanalysis/surface_gauss/catalog.html`). For years prior to 1948, the average monthly sea level pressure from 1948-1978 is used.

$pCO_{2,sw}$ is calculated from the modeled DIC field and the observed sea-surface alkalinity from the Global Ocean Data Analysis Project v2 (GLODAPv2) objectively mapped total alkalinity field. CO_2 system chemistry is handled with the CO2SYS calculator (Lewis & Wallace, 1998), using the observed monthly sea-surface temperature (SST) from reanalysis products, and the World Ocean Atlas monthly sea-surface salinity (SSS) climatology (Zweng et al., 2013), to compute the equilibrium constants. A suite of simulations is performed using several different SST reanalysis products, in order to take into account uncertainty in the reconstructed SST, which is most important for computing the CO_2 solubility α in equation (1) of the main text. These different simulations use SST reconstructions from the Hadley Centre (HadISST) (Rayner et al., 2003) (data available at `https://www.metoffice.gov.uk/hadobs/hadisst/index.html`), the Japan Meteorological Agency (COBE) (Ishii et al., 2005) (data available at `https://psl.noaa.gov/data/gridded/data.cobe.html`), and the National Oceanic and Atmospheric Administration extended reconstructed SST v5 (ERSSTv5) (Huang et al., 2015) (data available at `https://psl.noaa.gov/data/gridded/data.noaa.ersst.v5.html`). All of these products cover the global ocean at monthly resolution from at least 1890-2020. For years prior to 1890 (or the starting year of the individual SST product if earlier than 1890), a monthly average of the first 30 years of available data is used. The global mean SST trend for each product is shown in Figure S3.

The piston velocity K_w in equation (1) of the main text is parameterized as a quadratic function of wind speed (Wanninkhof et al., 2013)

$$K_w = a\,(1 - f_{ice})\left(u_{10}^2\right)\left(\frac{\mathrm{Sc}_{CO_2}}{660}\right)^{-0.5}, \tag{2}$$

where a is a coefficient with a value of 0.262 (for a piston velocity in cm hr^{-1} with wind speed in m s^{-1}), which was determined by the OCIM2-48L inversion. This values is very similar to the value of 0.251 suggested by (Wanninkhof et al., 2013). f_{ice} is the fractional sea ice cover (0 indicating open water and 1 indicating complete ice coverage), u_{10} is the 10-m wind speed in m s^{-1}, and Sc_{CO_2} is the temperature-dependent Schmidt number for CO_2. The 10-m wind speed u_{10} is calculated from the root mean square of 6-hour reanalysis wind speeds from the NCEP reanalysis product (Kalnay et al., 1996). The fractional ice cover is also taken from the NCEP reanalysis product, which covers the period 1948-2020. For years prior to 1948, u_{10} and f_{ice} are set to their monthly average value for the period from 1948-1978.

Model simulations cover the years 1780-2018 at a monthly resolution. The model is spun up to a seasonally-varying equilibrium using the average $p\mathrm{CO}_{2,air}$ from 1700-1780, which is 277 ppm when globally and annually averaged. Spin-up is accomplished using a Newton-Krylov solver to find the seasonally-varying cyclostationary steady-state (Li & Primeau, 2008). Then, the model is run forward from 1780-2020 using an Euler backward scheme with a time-step of 1 month. Six different model simulations are run using different combinations of external forcings. In the first three simulations (A–C, Table S1), $\mathrm{pCO}_{2,air}$ is varied but SST is held constant during the transient simulation from 1780-2020, while in the second set of simulations (D–F, Table S1), both the $\mathrm{pCO}_{2,air}$ and SST are varied.

All simulations use a time-varying gas transfer velocity based on varying winds and sea ice.

1.4. Effects of steady-state biology on the air-sea CO_2 fluxes

The results presented here use an abiotic model, which raises the question as to whether the inclusion of biological carbon cycling (as in the real ocean) would change the conclusions presented in this study. To assess whether including biological carbon cycling makes a difference, I created a twin simulation to simulation D, this time adding in biological carbon fluxes derived from the data-constrained biological pump model SIMPLE-TRIM DeVries and Weber (2017). The SIMPLE-TRIM model is a satellite-based observationally-constrained biological pump model that describes the biological cycling of organic carbon (both particulate and dissolved) due to net primary production in the euphotic zone, and the export and regeneration of organic carbon in the interior ocean. The model is constrained by observations of dissolved organic carbon (DOC) concentration, particulate organic carbon (POC) fluxes, and dissolved oxygen concentration. The model does not include $CaCO_3$ formation or dissolution.

Adding these biological fluxes to the model results in a biotic version of the model, which is described by the equation,

$$\frac{\partial \mathrm{DIC}}{\partial t} = \mathbf{A}\mathrm{DIC} - \frac{F_{air-sea}}{\delta z_1} + J_{bio}, \tag{3}$$

where J_{bio} are the biological carbon fluxes. The biotic model is solved using the same methods as the abiotic model. Adding the biological carbon cycling to the model changes the distribution of DIC, by up to 100 μmol kg^{-1} locally in the surface ocean. However, adding biology does not change the evolution of the air-sea CO_2 flux over time (Fig. S4).

Comparing the abiotic and biotic simulations, it is clear that the global air-sea CO_2 flux, and its variability over time, is virtually identical in both models (Fig. S4).

1.5. Comparison of CO_2 uptake to previous studies

The differences between the OCIM2-48L and the OCIM1 (DeVries, 2014) cause these studies to predict slightly different CO_2 uptake by the ocean. To examine these differences, I compared the global air-sea CO_2 fluxes in the current study with those from OCIM1 (Figure S5). The OCIM2-48L simulations A–C, which do not include SST variability, are the most directly comparable to the OCIM1 simulations, which also used a constant SST. However, it should be noted that the OCIM2-48L simulations A–C use a time-variable gas transfer velocity, while the OCIM1 simulations use a constant gas transfer velocity. CO_2 uptake in the OCIM1 is slightly larger, by $\sim$0.1 PgC yr^{-1}, than that in the OCIM2-48L simulations A–C (Fig. S5). The reason for this is primarily the deeper surface mixed layers used in the OCIM1, where winter maximum mixed layers were imposed in the model. The OCIM2-48L imposes annual average mixed layer depths, and thus the ocean takes up anthropogenic CO_2 at a slightly slower rate. It is not clear which formulation of the surface mixed layer depth is more appropriate for an annual-mean model that does not resolve the seasonal cycle of mixed layer shoaling and deepening, and so the $\sim$0.1 PgC yr^{-1} difference between the two different OCIM versions can be considered an additional source of structural uncertainty in the OCIM estimate of the magnitude of the oceanic CO_2 sink.

The magnitude of variability of the global air-sea anthropogenic CO_2 fluxes is similar in both the OCIM2-48L simulations A–C and the OCIM1 simulations (Fig. S5). The interannual variability is 0.08 PgC yr^{-1} in both the OCIM1 and OCIM2-48L, while the 5-year mean variability is 0.05 PgC yr^{-1} in both models. The pCO_2 forced variability is slightly larger in the OCIM1 due to its deeper mixed layers, which allows more of the ocean to come into equilibrium with the changing atmospheric CO_2, while the OCIM2-48L has additional high-frequency variability due to its changing gas transfer velocities, which were held constant in the OCIM1 simulations. This imparts some difference in the interannual variability of the OCIM2-48L simulations A–C and the OCIM1, with a correlation coefficient of 0.73 for the interannual variability. These differences are reduced when the 5-year smoothed variability is considered, where the correlation between the OCIM1 and OCIM2-48L (simulations A–C) is 0.83.

Figure S6 compares the column inventory of DIC accumulation in the OCIM2-48L simulations (A–C), and in the OCIM1 simulations (DeVries, 2014) for the period 1960-2010, and the DIC-based estimate of anthropogenic CO_2 accumulation from the extended multilinear regression approach (eMLR-C*) for the period 1994–2007 (Gruber et al., 2019). The OCIM2-48L has slightly higher DIC accumulation in the subpolar Atlantic and in the western boundary current of the North Atlantic Ocean compared to the OCIM1, as well as greater accumulation in the Antarctic region of the Southern Ocean (Fig. S6a-c). It has slightly less accumulation of DIC in most of the remaining low- to mid-latitude regions (Fig. 6c). Much of the difference can be attributed to the higher vertical resolution of the OCIM2-48L, which allows better resolution of topographic features such as the mid-Atlantic ridge, and could account for some of the reduction of the column inventory of DIC in the mid-North Atlantic (Fig. S6a). The remaining differences are tied to differences in circulation, particularly the deeper mixed layers in the OCIM1 which tend to accentuate storage in the mid-latitude storm tracks and mode water formation regions (Fig. S6b). Compared to the anthropogenic CO_2 accumulation estimated with the eMLR-C* approach, the OCIM2-48L has greater DIC accumulation in the North Atlantic and along the deep western boundary current, and less DIC accumulation in the South Atlantic and most of the tropical and subtropical oceans (Fig. S6d-f). The OCIM2-48L also has slightly higher DIC accumulation in the Pacific and Indian sectors of the Southern Ocean (Fig. S6f). These differences have been tied to changes in ocean circulation during the 1994–2007 period (Gruber et al., 2019).

1.6. Subsurface ocean heat content anomalies in the OCIM and observations

Subsurface temperature anomalies do not directly affect the air-sea CO_2 exchange (which depends only on the temperature at the sea surface), but the evolution of these anomalies provides a useful check on the consistency of the prescribed SST boundary condition with the assumed steady-state ocean circulation in the OCIM2-48L. To evaluate the evolution of subsurface temperature anomalies, a simulation was run with the OCIM2-48L to diagnose the subsurface temperatures that would evolve consistently with the prescribed SST boundary condition. This simulation solves the equation

$$\frac{dT_i}{dt} = \mathbf{A_{is}} T_s + \mathbf{A_{ii}} T_i, \tag{4}$$

where T_i is the interior (subsurface) temperature, T_s is the prescribed surface temperature, $\mathbf{A_{ii}}$ is the partition of the transport operator corresponding to the interior grid cells in the model, and $\mathbf{A_{is}}$ is the partition of the transport operator corresponding to transport between the surface layer and the interior. Equation 4 was solved at a cyclostationary steady-state for the preindustrial period, and then integrated to the present day using a 1-month time step with an Euler backward discretization. The calculation was repeated three times for each of the three SST products used here (Table S1).

The resulting modeled temperature field was used to calculate the global ocean heat content (OHC) for the upper 300 m of the ocean, which is approximately the mean depth affected by the eruption of Mt. Pinatubo in 1991 (Eddebbar et al., 2019). The OHC was calculated using the OCIM modeled temperature field, along with density and specific heat capacity calculated from annual mean temperature and salinity fields from the World Ocean Atlas (Locarnini et al., 2013; Zweng et al., 2013). The OHC reconstructed from the observed SST and steady-state OCIM2-48L circulation shows a reasonably good correspondence to the observations before and after the Pinatubo eruption (Figure S7). After hitting a peak around 1991, the upper-ocean OHC drops by ∼5-10 ZJ roughly 3 years after the Pinatubo eruption. This is within the range of responses found in the data-based reconstructions, which show a similar peak in upper-ocean OHC in 1991 followed by a drop of 6-21 ZJ roughly 3-4 years after the eruption. The OHC anomaly based on the temperature perturbation applied in the box model of (McKinley et al., 2020) is also shown in Figure S7 for comparison.

Table S1. Six different OCIM2-48L simulations using the atmospheric pCO_2 time history (see Fig. S2) and different combinations of sea-surface temperatures (SST), wind speed (u_{10}) and sea ice concentration (f_{ice}).

Simulation	$p\mathrm{CO}_{2,air}$	SST	u_{10} and f_{ice}
A	Variable	ERSSTv5 constant	NCEP variable
B	Variable	COBE SST constant	NCEP variable
C	Variable	HadISST constant	NCEP variable
D	Variable	ERSSTv5 variable	NCEP variable
E	Variable	COBE SST variable	NCEP variable
F	Variable	HadISST variable	NCEP variable

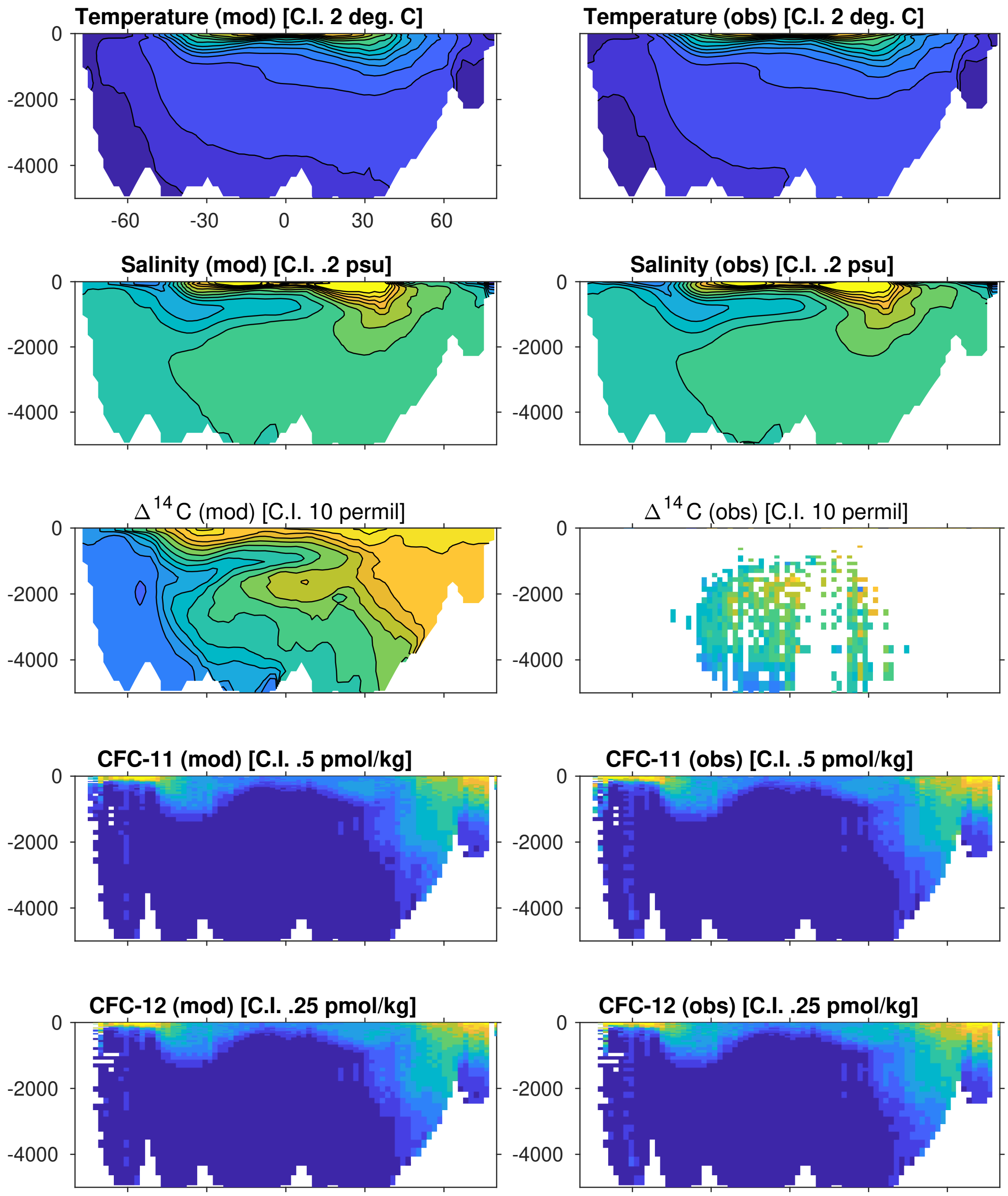

Figure S1. Atlantic basin-average tracer concentrations from the OCIM2-48L (left column) and observations (right column). Contour intervals for each plot are given in the title, and ranges are as follows: potential temperature (-2 to 28 °C), salinity (32.8 to 36.2 psu), Δ^{14}C (-200 to -40 ‰), CFC-11 (0 to 6 pmol kg^{-1}, and CFC-12 (0 to 3 pmol kg^{-1}). CFC concentrations are averaged over the entire period of collection at those times and locations that have CFC measurements. Δ^{14}C concentrations are shown for all locations in the model, and for those locations that have observations excluding those that have been identified as potentially contaminated by bomb ^{14}C.

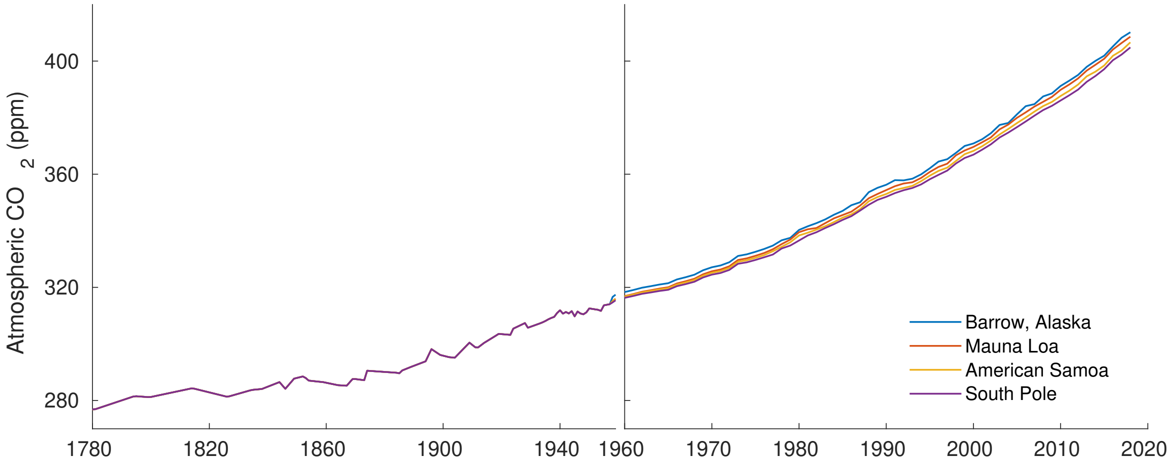

Figure S2. Annual-average atmospheric CO_2 concentration at four monitoring stations used to derive 3-dimensional maps of atmospheric pCO_2 for the OCIM2-48L simulations.

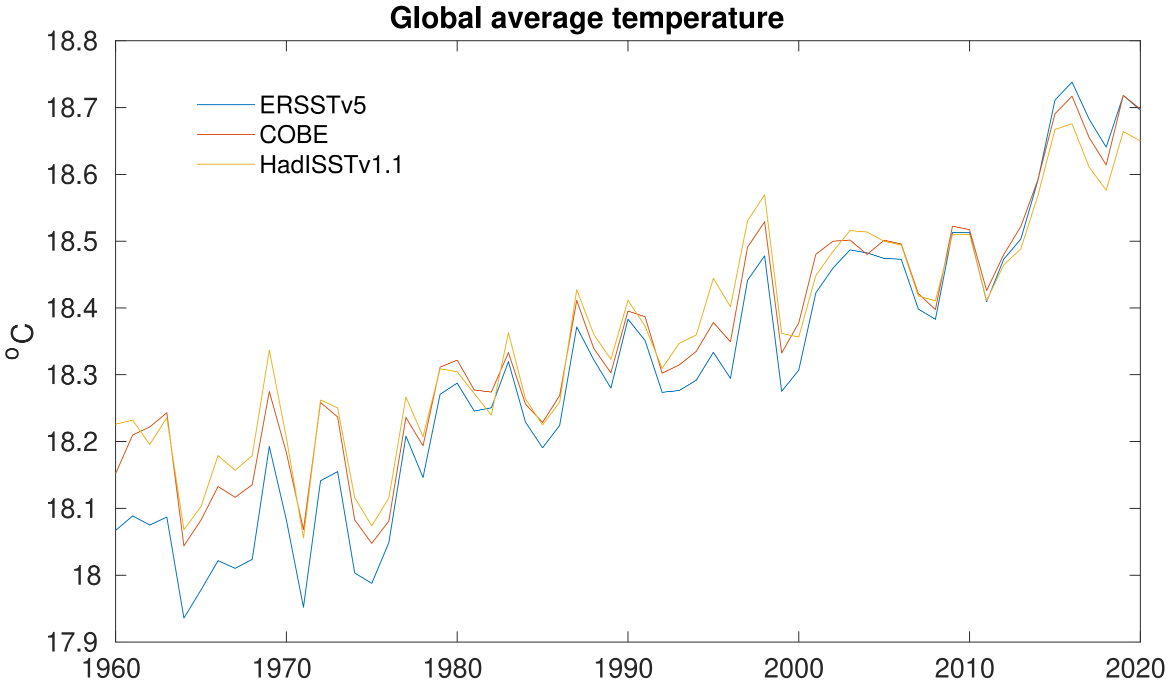

Figure S3. Global-mean SST from the three different SST products used in this study.

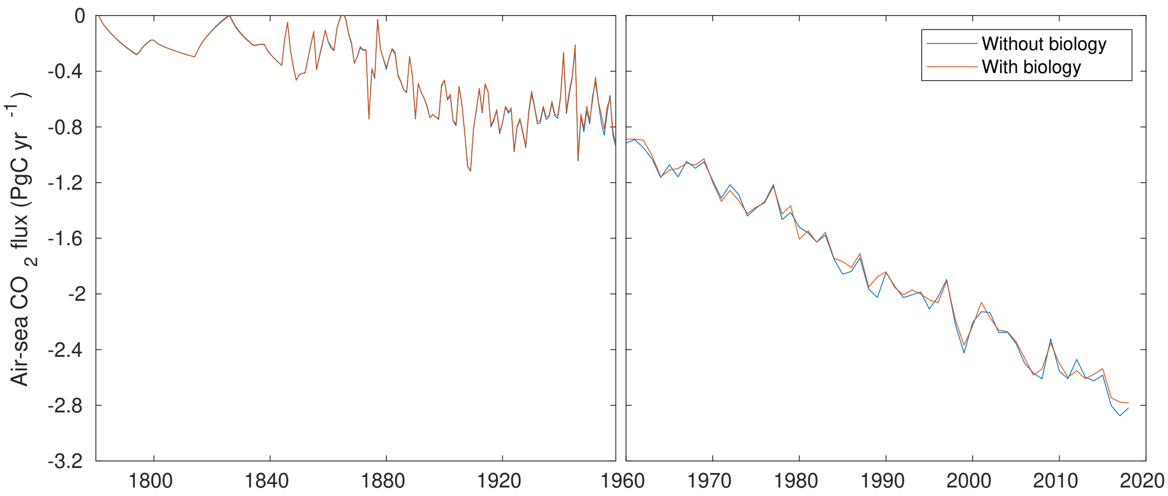

Figure S4. The temporal evolution of the global air-sea CO_2 flux in the abiotic model simulation D (without biology, blue curve), compared to that in a twin simulation with biology included (with biology, red curve). There is a small global air-sea flux of CO_2 in the preindustrial biotic simulation of $\sim$0.2 PgC yr^{-1} due to the burial of organic carbon, which is subtracted in order to make both simulations directly comparable.

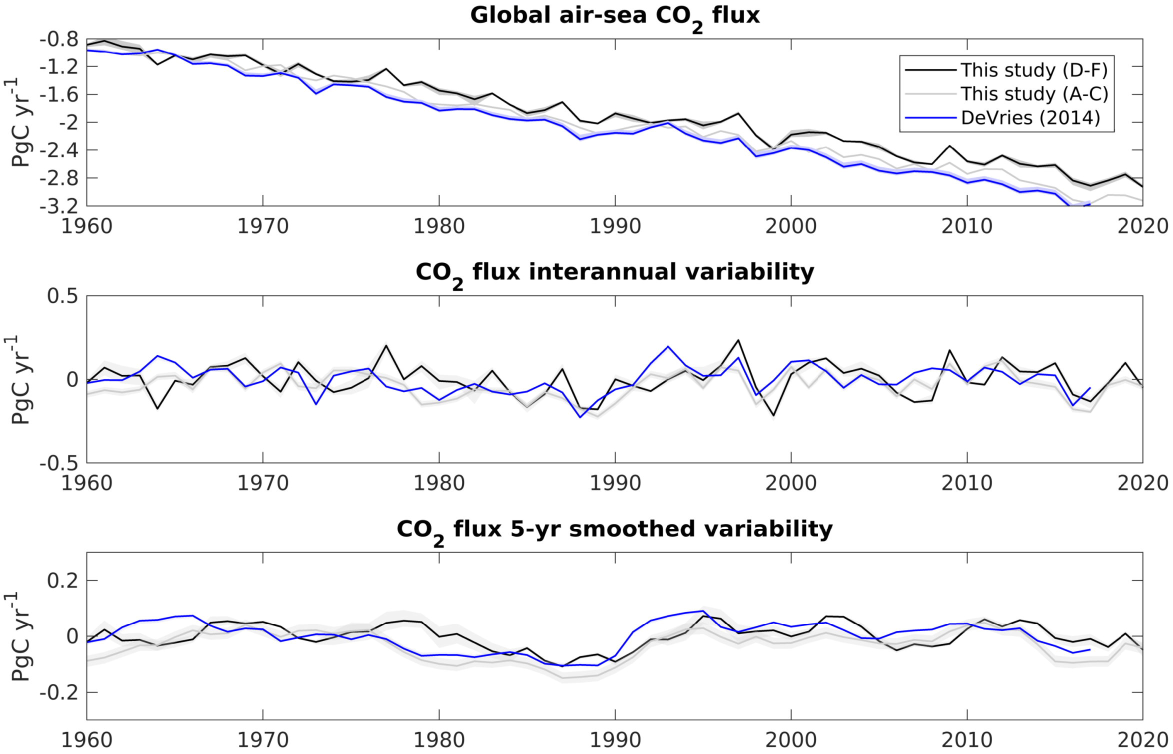

Figure S5. (a) Comparison of global air-sea CO$_2$ fluxes from 1960-2020 from the current study (OCIM2-48L simulations A–C in grey, simulations D–F in black) and the OCIM1 DeVries (2014). (b-c) The variability of the global air-sea CO$_2$ flux in the two studies, calculated by detrending the annual time-series shown in panel (a) using the same procedure as for main text Figure 4b-c.

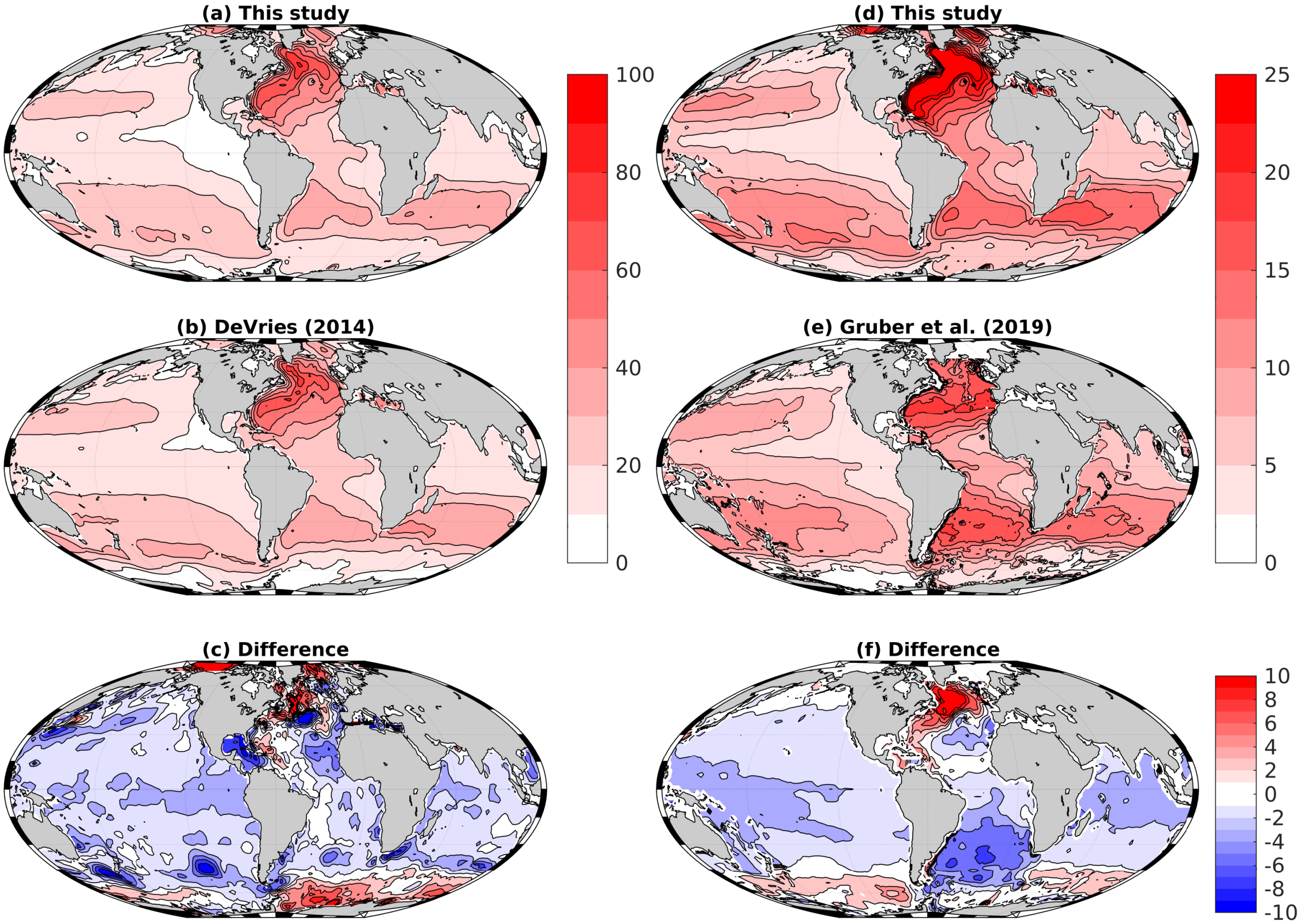

Figure S6. (a) Column inventory of DIC accumulation in the OCIM2-48L for 1960–2010 (average of simulations A–C; same as main text Fig. 3b but for the period 1960–2010). (b) Same as (a) but for the control simulation (CTL) of the OCIM1 DeVries (2014). (c) The difference between panels (a) and (b) (a-b). (d) Column inventory of DIC accumulation in the OCIM2-48L for 1994–2007 (average of simulations A–C; same as main text Fig. 3b but for the period 1994–2007). (e) Same as (d) but for the standard extended multilinear regression (eMLR) method of Gruber et al. (2019). (f) The difference between panels (d) and (e) (d-e). Panels (c) and (f) use the same colorbar, shown in panel (f).

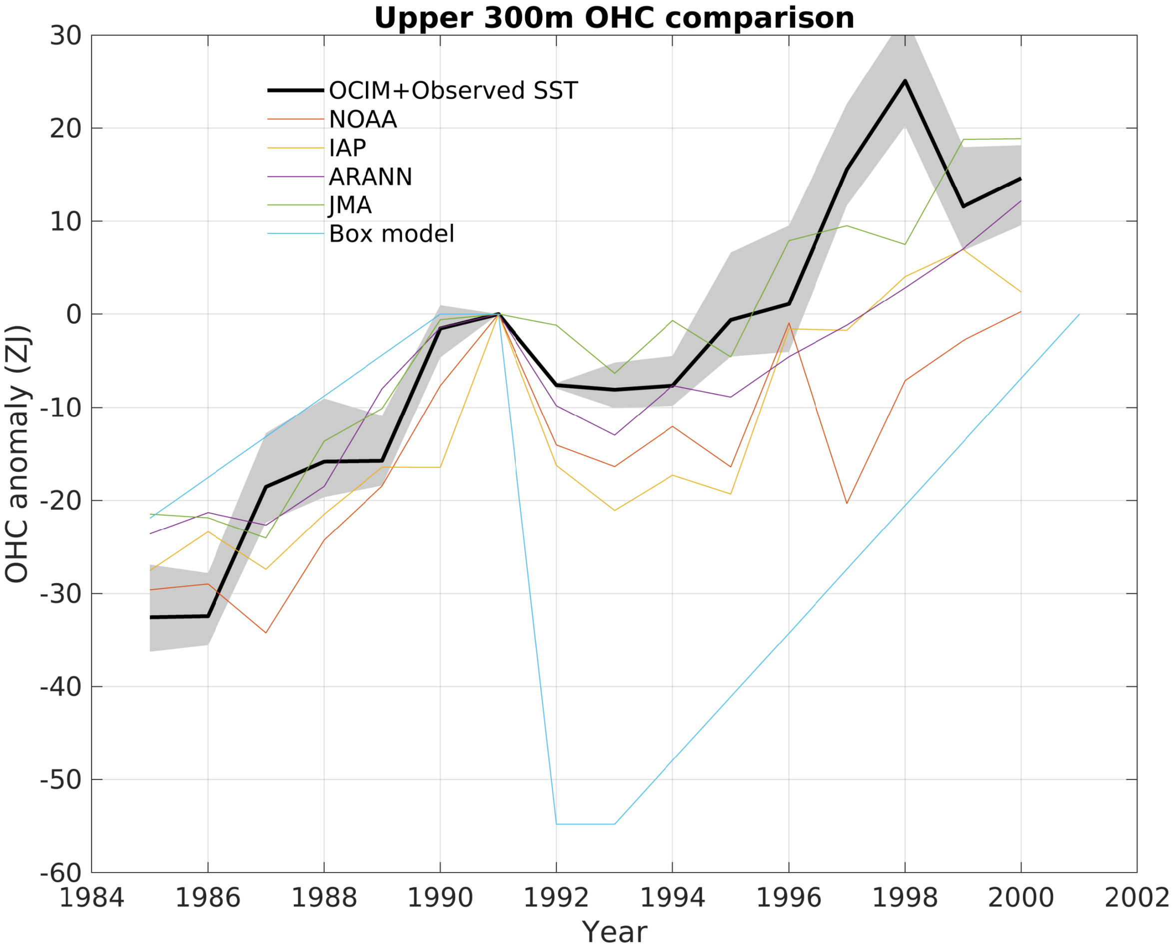

Figure S7. Ocean heat content (OHC) anomalies in the upper 300 m of the global ocean using the SST reconstructions and the OCIM2-48L circulation model (black line represents the mean of three simulations using three different SST products), compared with previous observation-based OHC reconstructions from the ARANN (Bagnell & DeVries, 2021), IAP (Cheng et al., 2017), NOAA (Levitus et al., 2012), and JMA (Ishii et al., 2017) products. Also shown for comparison is the OHC anomaly in the upper-ocean box model of McKinley et al. (2020). Each product has been scaled to have an OHC anomaly of 0 in the year 1991, the year of the Mt. Pinatubo eruption. Note 1 ZJ = 10^{21} J.

References

Bagnell, A., & DeVries, T. (2021). 20th century cooling of the deep ocean contributed to delayed acceleration of earth's energy imbalance. *Nature Communications*, *12*(1), 1–10.

Behringer, D., & Xue, Y. (2004). Evaluation of the global ocean data assimilation system at NCEP: The Pacific Ocean. In *Proc. eighth symp. on integrated observing and assimilation systems for atmosphere, oceans, and land surface.*

Cheng, L., Trenberth, K. E., Fasullo, J., Boyer, T., Abraham, J., & Zhu, J. (2017). Improved estimates of ocean heat content from 1960 to 2015. *Science Advances*, *3*(3), e1601545.

de Lavergne, C., Falahat, S., Madec, G., Roquet, F., Nycander, J., & Vic, C. (2019). Toward global maps of internal tide energy sinks. *Ocean Modelling*, *137*, 52–75.

de Lavergne, C., Vic, C., Madec, G., Roquet, F., Waterhouse, A. F., Whalen, C., . . . Hibiya, T. (2020). A parameterization of local and remote tidal mixing. *Journal of Advances in Modeling Earth Systems*, *12*(5), e2020MS002065.

DeVries, T. (2014). The oceanic anthropogenic CO_2 sink: Storage, air-sea fluxes, and transports over the industrial era. *Global Biogeochem. Cycles*, *28*, 631–647.

DeVries, T., & Holzer, M. (2019). Radiocarbon and helium isotope constraints on deep ocean ventilation and mantle-3he sources. *Journal of Geophysical Research: Oceans*, *124*(5), 3036–3057.

DeVries, T., & Primeau, F. (2011). Dynamically and observationally constrained estimates of water-mass distributions and ages in the global ocean. *J. Phys. Ocean.*, *41*, 2381–2401. doi: 10.1175/JPO-D-10-05011.1

DeVries, T., & Weber, T. (2017). The export and fate of organic matter in the ocean: New constraints from combining satellite and oceanographic tracer observations. *Global Biogeochemical Cycles*, *31*(3), 535–555.

Dlugokencky, E., Mund, J., Crotwell, A., Crotwell, M., & Thoning, K. (2020). *Atmospheric Carbon Dioxide Dry Air Mole Fractions from the NOAA GML Carbon Cycle Cooperative Global Air Sampling Network, 1968-2019, Version: 2020-07* (Tech. Rep.). Retrieved from `https://doi.org/10.15138/wkgj-f215`

Eddebbar, Y. A., Rodgers, K. B., Long, M. C., Subramanian, A. C., Xie, S.-P., & Keeling, R. F. (2019). El niño–like physical and biogeochemical ocean response to tropical eruptions. *Journal of Climate*, *32*(9), 2627–2649.

Graven, H., Gruber, N., Key, R., Khatiwala, S., & Giraud, X. (2012). Changing controls on oceanic radiocarbon: New insights on shallow-to-deep ocean exchange and anthropogenic CO_2 uptake. *Journal of Geophysical Research: Oceans*, *117*(C10).

Gruber, N., Clement, D., Carter, B. R., Feely, R. A., van Heuven, S., Hoppema, M., ... Wanninkhof, R. (2019). The oceanic sink for anthropogenic CO_2 from 1994 to 2007. *Science*, *363*(6432), 1193–1199.

Guilderson, T., Schrag, D., Fallon, S., Dunbar, R., Kilbourne, K., & Prouty, N. G. (2005). *Surface Water Radiocarbon (Delta14C) Reconstructed from Reef-Building Zooxanthellate Corals from 1751-2004* (Tech. Rep.). Oak Ridge, Tennessee. Retrieved from `http://cdiac.ornl.gov/ftp/oceans/coralC14_data/`.

Huang, B., Banzon, V. F., Freeman, E., Lawrimore, J., Liu, W., Peterson, T. C., ... Zhang, H.-M. (2015). Extended reconstructed sea surface temperature version 4 (ERSST. v4). Part I: Upgrades and intercomparisons. *Journal of climate*, *28*(3), 911–930.

Ishii, M., Fukuda, Y., Hirahara, S., Yasui, S., Suzuki, T., & Sato, K. (2017). Accuracy of global upper ocean heat content estimation expected from present observational data sets. *Sola*, *13*, 163–167.

Ishii, M., Shouji, A., Sugimoto, S., & Matsumoto, T. (2005). Objective analyses of sea-surface temperature and marine meteorological variables for the 20th century using ICOADS and the Kobe collection. *International Journal of Climatology: A Journal of the Royal Meteorological Society*, *25*(7), 865–879.

Kalnay, E., Kanamitsu, M., Kistler, R., Collins, W., Deaven, D., Gandin, L., … Joseph, D. (1996). The NCEP/NCAR 40-year reanalysis project. *Bulletin of the American meteorological Society*, *77*(3), 437–472.

Large, W. G., McWilliams, J. C., & Doney, S. C. (1994). Oceanic vertical mixing: A review and a model with a nonlocal boundary layer parameterization. *Reviews of Geophysics*, *32*(4), 363–403.

Levitus, S., Antonov, J. I., Boyer, T. P., Baranova, O. K., Garcia, H. E., Locarnini, R. A., … others (2012). World ocean heat content and thermosteric sea level change (0–2000 m), 1955–2010. *Geophysical Research Letters*, *39*(10).

Lewis, E., & Wallace, D. (1998). *Program developed for CO_2 system calculations* (Tech. Rep.). Oak Ridge, Tennessee: Carbon Dioxide Information Analysis Center, Oak Ridge National Laboratory.

Li, X., & Primeau, F. W. (2008). A fast Newton–Krylov solver for seasonally varying global ocean biogeochemistry models. *Ocean Modelling*, *23*(1-2), 13–20.

Locarnini, R., Mishonov, A., Antonov, J., Boyer, T., Garcia, H., Baranova, O., … Seidov, D.

(2013). World Ocean Atlas 2013, Volume 1: Temperature. In S. Levitus & A. Mishonov (Eds.), . NOAA Atlas NESDIS 73.

Macfarling Meure, C., Etheridge, D., Trudinger, C., Steele, P., Langenfelds, R., Van Ommen, T., … Elkins, J. (2006). Law Dome CO_2, CH_4 and N_2O ice core records extended to 2000 years BP. *Geophysical Research Letters*, *33*(14).

McKinley, G. A., Fay, A. R., Eddebbar, Y. A., Gloege, L., & Lovenduski, N. S. (2020). External forcing explains recent decadal variability of the ocean carbon sink. *AGU Advances*, *1*(2), e2019AV000149.

Olsen, A., Key, R. M., van Heuven, S., Lauvset, S. K., Velo, A., Lin, X., … Suzuki, T. (2016). The Global Ocean Data Analysis Project version 2 (GLODAPv2) – an internally consistent data product for the world ocean. *Earth System Science Data*, *8*(2), 297–323. Retrieved from `https://essd.copernicus.org/articles/8/297/2016/` doi: 10.5194/essd-8-297-2016

Rayner, N., Parker, D. E., Horton, E., Folland, C. K., Alexander, L. V., Rowell, D., … Kaplan, A. (2003). Global analyses of sea surface temperature, sea ice, and night marine air temperature since the late nineteenth century. *Journal of Geophysical Research: Atmospheres*, *108*(D14).

Wanninkhof, R., Park, G.-H., Takahashi, T., Sweeney, C., Feely, R., Nojiri, Y., … Khatiwala, S. (2013). Global ocean carbon uptake: magnitude, variability and trends. *Biogeosciences*, *10*(3), 1983–2000.

Zweng, M., Reagan, J., Antonov, J., Locarnini, R., Mishonov, A., Boyer, T., … Biddle, M. (2013). World Ocean Atlas 2013, Volume 2: Salinity. In S. Levitus & A. Mishonov (Eds.), . NOAA Atlas NESDIS 74.